Extreme Mechanics Letters 24 (2018) 58–65

Contents lists available at ScienceDirect

Extreme Mechanics Letters

journal homepage: www.elsevier.com/locate/eml

Mechanical behavior of 3D printed biomimetic Koch fractal contact and interlocking

Mona Monsef Khoshhesab, Yaning Li *

Department of Mechanical Engineering, University of New Hampshire, Durham, NH, 03824, USA

ARTICLE INFO

Article history:
Received 23 May 2018
Received in revised form 14 September 2018
Accepted 30 September 2018
Available online 12 October 2018

Keywords:
Koch fractal
3D-printing
Topological interlocking
Contact

ABSTRACT

Inspired by the hierarchical/fractal topological interlocking in nature, Koch fractal interlocking with different numbers of iteration *N* are designed. To better understand the mechanics of fractal interlocking, the designs are also fabricated via a multi-material 3D printer. Mechanical experiments and finite element (FE) simulations are performed to further explore the mechanical performance of the new designs. Analytical model is also developed to capture the deformation mechanisms of the fractal interlocking through contact. It is found that the load-bearing capacity of Koch fractal interlocking can be effectively increased via fractal design. However, the mechanical responses of fractal interlocks are also sensitive to imperfections, such as the gap between the interlocked pieces and the rounded tips. When fractal complexity increases, the mechanical properties will become more and more sensitive to the imperfection and eventually, the influences from imperfection can even become dominant. By considering the influences of imperfection, the theoretical model predicts the existence of an optimal level of fractal complexity for maximizing mechanical performance.

1. Introduction

In nature, during years of evolution, many biological systems develop complicated geometrical and material heterogeneity across several length scales to achieve light weight and high mechanical performance [1–6]. Generally, hierarchical heterogeneity can be achieved via two different mechanisms: (1) variation of nano/micro structures at different length scale, such as bones and sea shells [7–9] and (2) self-similarity via fractal geometry, such as gecko feet [10,11] and biological sutures [12–14]. Fractal plays an important role in the second category to achieve heterogeneity across several length scales. The Koch fractal interlocking explored in this investigation falls in the second category. It is one type of fractal-induced self-similar mechanical interlocking, which provides one option of designing hierarchical geometric heterogeneity in any material system.

Due to self-similarity, fractals exhibit great complexity driven by simplicity [15–18]. Therefore, fractals are ubiquitous in nature, such as the structure of Romanesco broccoli, frost crystals occurring naturally on cold glass [19]. Fractals not only can model complex forms, but also act as a bridge between regular geometries to irregular ones [3,20,21]. Fractals are also widely used in engineering area. For example, in architecture engineering, fractals are used to design bio-inspired constructions [22–24]; in electrical engineering, they are used to produce electronic circuit with chaotic behavior [25]; in biomedical engineering, fractals are used to model and measure tumor and irregular distribution of collagen fibers in biological tissue [26].

Topological interlocking plays a critical role in joining similar/dissimilar materials and structures, in both adhesive science and engineering [27–30] and plasticity and creep of ductile metals [30,31]. The interlocked segments are constrained in their movement by the neighboring ones, providing stability and allowing for restricted locomotion of neighboring segments [17,32,33]. Compared with bonding via adhesive materials or mechanical fasteners, mechanical interlocking has a similar function but is simpler and more robust in terms of manufacturing [24,17]. Recently, topological interlocking has been shown to be an effective method to create a new class of architectured materials [8,33–35]. For example, the interlocking mechanism of dove-tail shaped building blocks was investigated through experimental, numerical and theoretical models [33,36–39]; and composite mechanical models of single waved sutures [12] and hierarchical sutures were also developed [2,12].

Examples of hierarchical/fractal interlocks in biological systems include sutural interlock on the carapace of red-eared turtle [40], the cranial suture of a white-tailed deer (Fig. 1a), the sutures in fossil ammonite [2] (Fig. 1b), the linking girdle of diatom (Fig. 1c), and the seed coat of common millet [41]. It is known that the hierarchical/fractal geometry is the key to achieve optimal mechanical properties and function of these interlocks. However, it is not well understood why the cranial suture of human being develops from a

* Corresponding author.
E-mail address: Yaning.Li@unh.edu (Y. Li).

https://doi.org/10.1016/j.eml.2018.09.003
2352-4316/

simple straight line to a complicated zigzag pattern during growth from infant to adult [14,42–44], why the complexity of ammonite suture consistently increases within several mass extinctions [18], and whether there is a limitation of geometry complexity in these biological systems.

To address these questions, recently, composite mechanical models of biological sutures with different waveforms were extensively explored [2,12,41,46–51]. The triangular tooth geometry was proved to be the optimized geometry to maximize strength and efficiency in load transmission [12,50,51]. Also, the mechanical properties have great sensitivity to geometric hierarchy [5,9,12,14,46,48]. For examples, it was found that by increasing the number of hierarchy, the overall stiffness, strength and fracture toughness of hierarchical sutures can be tuned by orders of magnitude [41,48,49,51].

In this investigation, the primary goal is to design Koch fractal interlocking and explore the influences of number of hierarchy, material properties, and geometric imperfection on the overall mechanical properties of the designs. Design principles of fractal interlocking will be developed, which will provide insights to develop optimized design for joining similar/dissimilar materials through topological interlocking.

2. Mechanical model and results

2.1. Design of Koch fractal interlocking

Fractal, named by Mandelbrot [3], as one of the youngest non-Euclidean geometric concepts [52] which uses simple algorithms to design complex forms. As one of the first mathematically described fractals, Koch curve was proposed by Helge von Koch [53] in 1904 as an example of a non-differentiable curve. It was generated via an iterated function system (IFS) with the number of iteration defined as N. It is initiated (at zero iteration, $N = 0$) from a line with length of $\boldsymbol{a_0}$. In the first iteration ($N = 1$), the middle $\boldsymbol{a_0}/3$ segment of the line is substituted by two segments of the same size but are rotated up for 60° as shown in Fig. 1d and the total length of the curve would be $4\boldsymbol{a_0}/3$. In the similar manner, the total arc length of Koch fractal in each order of hierarchy N can be defined as $\boldsymbol{L_N} = \boldsymbol{a_0}\,(\boldsymbol{4/3})^{\boldsymbol{N}}$.

Thus, to satisfy the definition of Koch fractal, the smallest section length a_N of the Nth order Koch curve is related to a_0 and N as:

$$a_N = \frac{a_0}{3^N}. \tag{1}$$

Then, the total arc length L_N of the Nth order Koch curve is related to a_0 and N as:

$$L_N = 4^N a_N = a_0\,(4/3)^N\,. \tag{2}$$

Eq. (2) shows that the total arc length L_N experiences exponential growth with N. Full differentiation of Eq. (2) gives:

$$dL_N = \frac{\partial L_N}{\partial a_0} da_0 + \frac{\partial L_N}{\partial N} dN, \tag{3}$$

Eqs. (1)–(3) yield:

$$dL_N = \left(\frac{4}{3}\right)^N da_0 + \ln\frac{4}{3} L_N dN = L_N\left(\frac{da_0}{a_0} + \ln\frac{4}{3} dN\right), \tag{4}$$

Eq. (4) shows that the growth rate of L_N is actually proportional to the current value of L_N, indicating the exponential growth of L_N with N.

In applying the Koch fractal concept in practical design, imperfections are introduced to disturb the ideal curve. For example, in order to avoid potential stress concentration at the tooth tips, all tips were rounded by radius r_N (shown in Fig. 1d and e). To ensure self-similarity, r_N is a function of N through $r_N = ca_N (0 < c < 1)$. Also, A small gap g between the two boundaries from the top and bottom pieces was introduced, as shown in Fig. 1e. To define g, first the Koch curve was rounded with radius r and then offset by g and defined the top part of Koch layer. Therefore, the geometry of the Koch fractal interlocking is determined by four independent geometry parameters: a_0, N, g, c in addition to friction coefficient μ.

2.2. Mechanical experiments on 3D printed specimens

Specimens of Koch fractal interlocking of $N = 2$, 3 and 4 and with $g = 0.2$ mm, and $r_N = 0.07a_N$ were designed and 3D printed via a multi-material 3D printer (Objet Connex 260). The major parts of the specimens were printed as VeroWhite and are shown in Fig. 2a. In order to accurately control the gap between the top and bottom pieces of the specimen, and facilitate the alignment of the two pieces, a soft rubbery material (TangoBlackPlus) was initially printed between the small gap of the specimen, so that the two pieces are well positioned. Quasi-static mechanical experiments were performed (with details provided in **Methods** section) under uni-axial tension. For repeatability, for each N, three identical specimens were printed and tested. The load–displacement curves of the three designs are compared in Fig. 2b (the thickness of the curves represents the variation from the three different tests for each N).

Fig. 2b shows that generally, each curve has two peaks. The first load drop after the first peak indicates the failure of the soft adhesive layer. The effects of the layer properties on the first peak were studied via systematic FE simulations in [54]. Then after the layer fails, the designs gain strength via fractal-induced contact and interlocking. After the second peak, the design starts to lose interlocking. Also, it can be seen that when N increases, both peaks increase. The second peak increases more dramatically with more improvement from $N = 2$ to $N = 3$ than from 3 to 4. Fig. 2c shows the interlocking between teeth at different levels for different Ns.

The damage of the adhesive layer dominates the behavior of the first peak, while the fractal interlocking is the dominant mechanism for the second peak. To focus on understanding the mechanics of Koch fractal contact and interlocking, for Koch fractal interlocking with $N = 2$, 3 and 4, 3D FE models with gaps instead of adhesive layer were developed. Elasto-plastic material model was used for VeroWhitePlus (details are provided in the **Methods** section). By using the friction coefficient $\mu = 0.01$ in all simulations, the FE results of the three designs captures the second peak of the experimental curves, as shown in Fig. 3a.

The FE results of the contact areas of the three cases are also output as functions of the overall displacement δ and are compared in Fig. 3b. The evolution of the contact area for the Koch fractal interlocking indicates three stages in deformation: Stage I ($\delta < g$), in this stage, no contact happens due to the small gap g; Stage II ($g < \delta < \frac{g}{\cos 60^\circ} = 2g$), only some of the flat surfaces from the top and bottom pieces are in contact; Stage III ($\delta > \frac{g}{\cos 60^\circ} = 2g$), some slant surfaces are also in contact. For the case of $N = 2$, only slant surfaces are in contact, so the force is zero in both Stages I and II, suddenly increases to a certain number when entering into Stage III. For the cases of $N = 3$ and 4, the contact area suddenly increases to a non-zero value when entering into Stage II, but gradually increases from Stage II to Stage III. This is because of the deformation of teeth. If the teeth are ideally rigid, a sudden increase in contact area is also expected when entering Stage III.

The FE contours of von Mises stress for the three cases at two different overall displacements ($\delta = 0.15$ mm, and $\delta = 0.35$ mm) are shown in Fig. 3c. It is shown that the loads concentrate around the area of contact and when N increases, the loads are more uniformly distributed along the fractal interface.

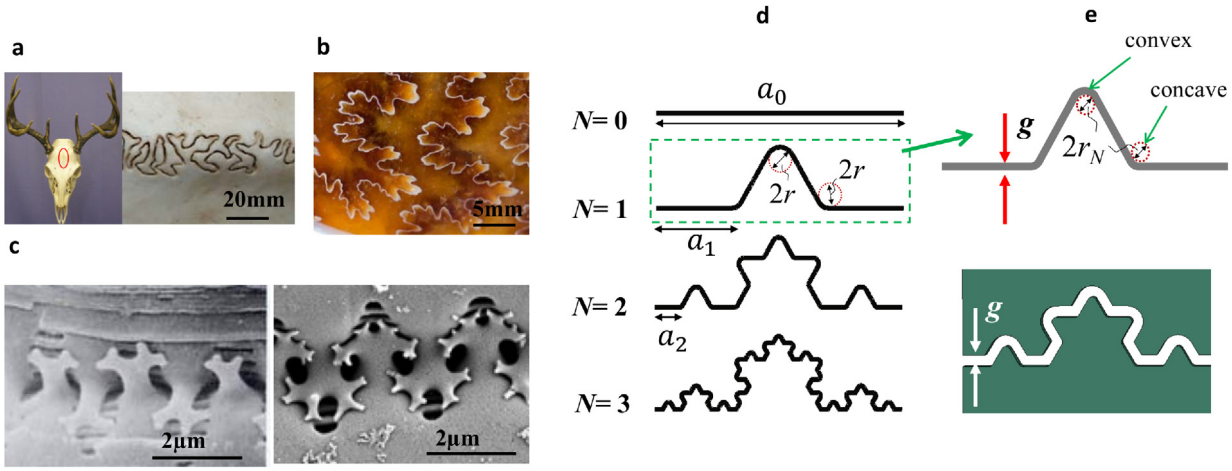

Fig. 1. Examples of hierarchical interlocking in nature: (a) cranial sutures in deer's skull, (b) ammonite suture [2] (c) diatom linking girdles [45], (d) Koch fractal design for $N = 0$, 1, 2 and 3, and (e) some details of the Koch fractal interlocking.

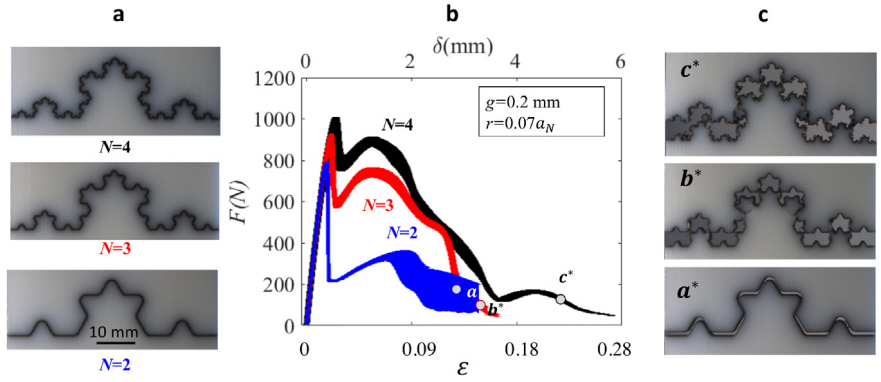

Fig. 2. (a) The joining zone of 3D-printed specimens with adhesive layer with $g = 0.2$ mm, $r_N = 0.07a_N$; (b) experimental force-strain/displacement response of Koch fractal contact model with an adhesive layer (TangoBlackPlus); and (c) the failed/deformed specimens shown in different stages of contact.

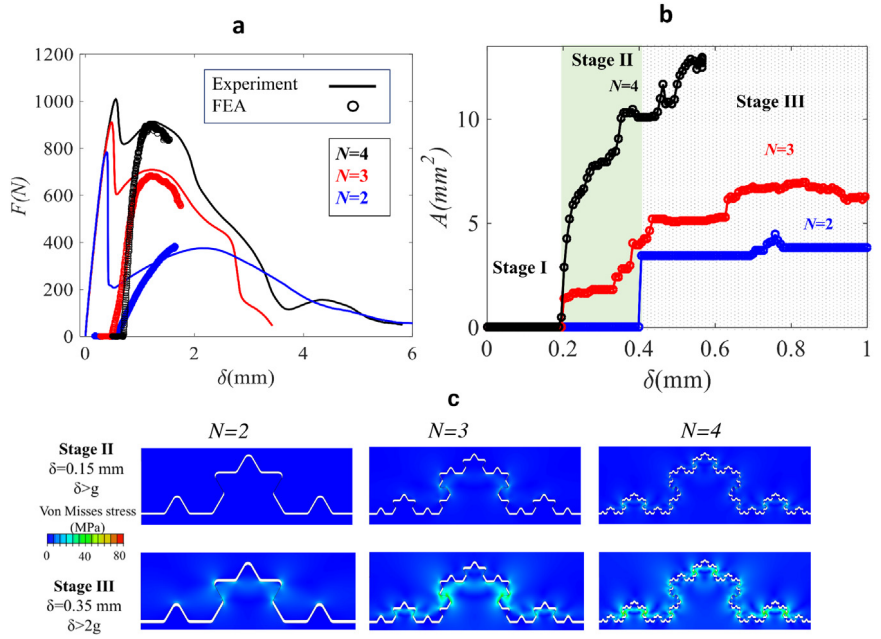

Fig. 3. (a) Comparison between FE models and experimental results. (b) contact area-displacement is shown when $N = 2$, 3 and 4. (c) FE contours of von Mises stress at stages II and III for $N = 2$, 3 and 4.

2.3. Mechanics for Koch fractal contact/interlocking

Based on the experimental and FE results, to further quantify the mechanical behavior of Koch fractal interlocking. Analytical mechanical model of the Koch fractal contact/interlocking is developed in this section.

Contact between flat and slant surfaces. The load bearing capacity of fractal interlocking for different Ns is achieved via contact along the boundaries of the top and bottom pieces. The representative volume element (RVE) of each N is shown in Fig. 4a. The RVEs for different Ns have the same width w and the same amplitude L. Since the fractal boundary is composed of flat (in blue) and slant (in red) segments, as shown in Fig. 4b ($N = 3$, as an example), the fundamental contact mechanism is the contact between two pieces with a flat contact surface, and a slant contact surface. Specifically, for Koch fractal contact, the slant contact surface forms a 60 degree angle with the horizontal direction, as shown in Fig. 4b.

The geometric model and the free body diagram for the basic contact problem with slant surface is shown in Fig. 4b, where the length of the model is L (it is the same as the amplitude of the Koch fractal design, as shown in Fig. 4a), the length of the slant surface is a and the angle between the slant surface and horizontal direction is 60 degrees. A local coordinate $\boldsymbol{n} - \boldsymbol{t}$ is defined with $\boldsymbol{t}$-axis along the contact surface, and $\boldsymbol{n}$-axis normal to the contact surface. Assume the far-field compressive force is F_s, and the contact-induced normal force on the contact surface is F_n, and the tangential force on the contact surface is F_t, the equilibrium of the top piece yields:

$$F_s = F_n \cos 60^\circ + F_t \sin 60^\circ. \tag{5}$$

By defining f_s, f_n and f_t as forces per unit length and based on the Coulomb's law of friction, Eq. (5) can be rewritten as:

$$f_s = f_n \left(1 + \mu \tan 60^\circ\right). \tag{6}$$

where μ is the static/kinetic friction coefficient. The normal deflection δ_n around the contact area is related to the overall displacement δ_s at the boundary as:

$$\delta_n = \delta_s \cos 60^\circ. \tag{7}$$

Thus, by assuming linear elastic constitutive behavior, the far-field traction–displacement relation $f_s - \delta_s$ can be obtained via the local normal traction–displacement relation $f_n - \delta_n$ in the contact area as:

$$f_s = k_n \left(1 + \mu \tan 60^\circ\right) \cos 60^\circ \delta_s, \tag{8}$$

where $k_n = E\frac{t}{L}$, in which L is the length of the model of a flat segment, t is the out of plane thickness and E is the Young's modulus of the base material. This model was derived under the assumption that there is no relative sliding between the slant surfaces in contact, so that the overall load–displacement behavior is the same as that of the bulk material of each piece.

By hierarchically applying this basic contact model for slant surfaces with no relative sliding via the Koch geometry, a theoretical model to predict the overall traction–displacement relation of Koch interlocking can be derived. Assume the vertical force applied at the boundaries of the Nth order Koch fractal interlock is $F(N)$, the force–displacement relations of the three stages can be expressed as:

$$\textbf{Stage I}: \; F(N) = 0; \qquad \delta < g \tag{9}$$

$$\textbf{Stage II}: F(N) = f_n a'_N \, n_f^{c[N]}; \qquad g < \delta < 2g \tag{10}$$

$$\textbf{Stage III}: (N) = f_s a'_N \, n_s^{c[N]} + f_n a'_N n_f^{c[N]}; \qquad \delta > 2g \tag{11}$$

where , $n_f^{c[N]}$ and $n_s^{c[N]}$ are the number of flat and slant segments in contact, respectively. $n_f^{c[N]}$ and $n_s^{c[N]}$ will be determined hierarchically as the following. a'_N is the contact length of one segment for Koch fractal interlocking at hierarchy N. For the ideal Koch fractal geometry (i.e. $g = r_N = 0$), $a'_N = a_N$; for cases with non-zero g and r_N, a'_N is determined by a_N, g and c (details are provided in the supporting information **S2**).

Determine contact area via self-reproducing mechanism. Due to the self-similarity of Koch fractal geometry, for Koch curves with $N > 2$, the geometry can be decomposed into six units with the geometry of $N = 1$ rotating counter-clockwise to the horizontal direction with six different angles (0°, +60°/−60°, +120°/−120° and 180°), as shown in Fig. 5a. The six units (each color represents one unit) are shown in Fig. 5b, named as units S_{0°, S_{60°, $S_{\pm 60^\circ}$ $S_{\pm 120^\circ}$, S_{180°, respectively. Due to symmetry, S_{+60° and S_{-60° behave the same, and S_{+120° and S_{-120° behave the same. Therefore, total four categories of units exist (Fig. 5b).

According to this categorization, Koch fractal with order N can be decomposed into units S_{0°, S_{60°, S_{120°, S_{180°. Thus, a vector $\boldsymbol{m}^{[N]}$ can be defined, representing the number of each unit in the Nth order RVE is x, y, z and k, respectively, i.e.

$$\boldsymbol{m}^{[N]} = \begin{bmatrix} x \\ z \\ y \\ k \end{bmatrix}^{[N]}. \tag{12}$$

Fig. 5b shows that from $N-1$ to N hierarchy, each S_{0° section will generate two S_{0° sections, and two S_{60° sections, but no S_{120° and S_{180° segments; each S_{60° section will generate one S_{0° section, two S_{60° sections, and one S_{120° section; each S_{120° section will generate one S_{60° section, two S_{120° sections, and one S_{180° section; and each S_{180° section will generate two S_{120° sections and two S_{180° sections in $[N]$ order hierarchy. Thus, due to self-similarity, the iterative relation of the number of each section at two neighboring hierarchies can be related via a reproducing matrix $\boldsymbol{R}$ as:

$$\boldsymbol{m}^{[N]} = \boldsymbol{R}\boldsymbol{m}^{[N-1]}, \text{ where } \boldsymbol{R} = \begin{bmatrix} 2 & 1 & 0 & 0 \\ 2 & 2 & 1 & 0 \\ 0 & 1 & 2 & 2 \\ 0 & 0 & 1 & 2 \end{bmatrix}. \tag{13}$$

By taking the first row as an example, matrix $\boldsymbol{R}$ means that S_{0° units in N hierarchy are generated from S_{0° and S_{60° in $N-1$ hierarchy, with two from S_{0°, one from S_{60° and none from S_{120° and S_{180°, as gives the first row of $\boldsymbol{R}$ as (2, 1, 0,0).

Among all flat and slant segments, only some of them are in contact/interlocking. We define a vector $\boldsymbol{n}^c$ to represent the number of segments in contact as:

$$\boldsymbol{n}^{c[N]} = \begin{bmatrix} n_f^c \\ n_s^c \end{bmatrix}^{[N]}, \tag{14}$$

where, n_f^c and n_s^c represent the numbers of flat and slant segments in contact, respectively.

Thus, the total number of flat and slant segments in contact can be determined via a contact matrix $\boldsymbol{C}$ as:

$$\boldsymbol{n}^{[N]} = \boldsymbol{C}\boldsymbol{m}^{[N]}, \text{ where } \boldsymbol{C} = \begin{bmatrix} 0 & 0 & 1 & 2 \\ 0 & 1 & 2 & 2 \end{bmatrix}. \tag{15}$$

Fig. 5c clearly explains that each S_{0° unit does not generate any segments in contact under uniaxial tension; each S_{60° unit only generates one slant segments in contact; each S_{120° unit generates one flat and two slant segments in contact; and each S_{180° unit generates two flat and two slant segments in contact.

Based on Eqs. (1)–(15), the effective load–displacement behavior of Koch fractal interlocking with all different parameters can be predicted. By taking the case of $N = 3$ as an example, the influences of the small gap g and friction coefficient μ on the overall force (F) and displacement (δ) relation are quantified via the theoretical model. Fig. 6a shows that for the perfect model of $g = r = \mu = 0$,

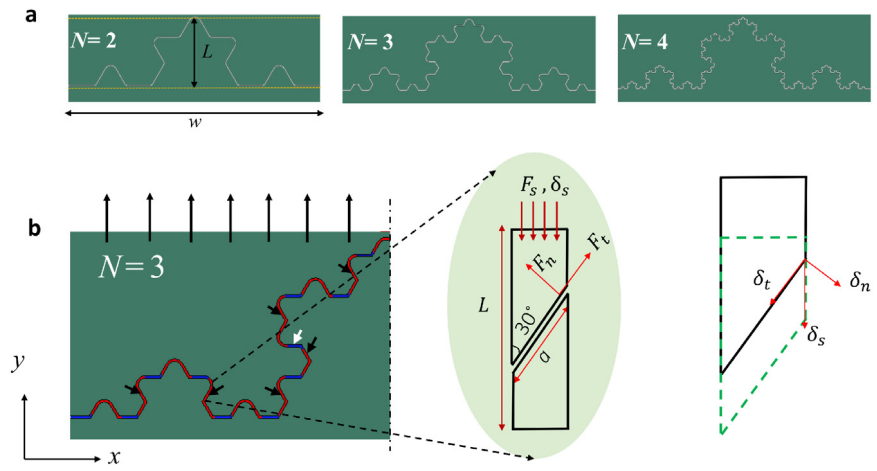

Fig. 4. (a) Geometry of Koch fractal interlocking with gaps for $N = 2$, 3 and 4; (b) categorizing slant (red) and flat (blue) segments for $N = 3$ case; (black and white arrows show slant and flat segments in contact, respectively), and the free body diagram of the top piece of a pair of slant segments in contact . (For interpretation of the references to color in this figure legend, the reader is referred to the web version of this article.)

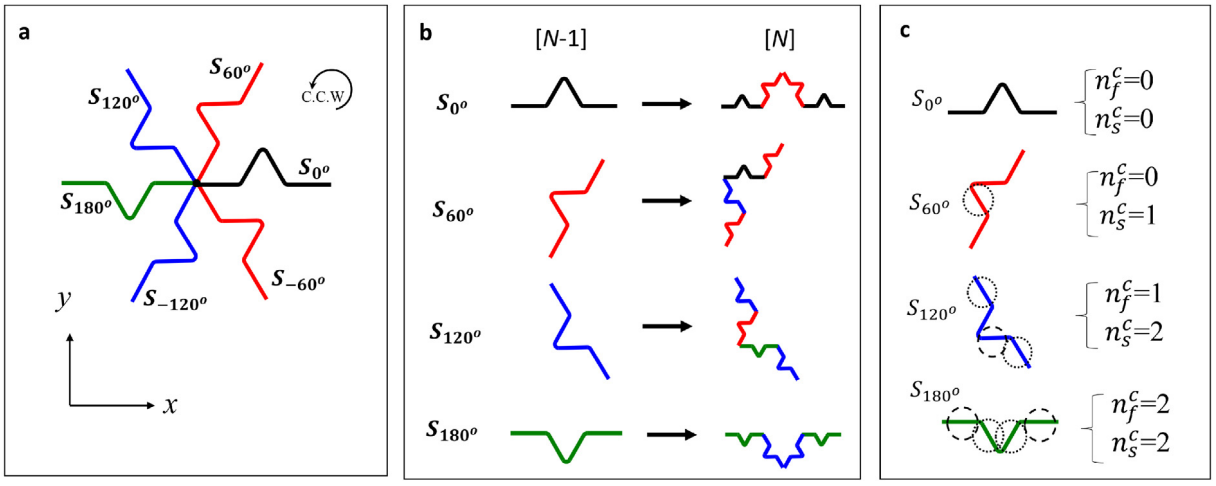

Fig. 5. (a) The six units (four categories represented by four colors) with $N = 1$ geometry S_{0°, S_{60°, S_{120°, S_{180°, S_{-120°, S_{-60°, rotating counter-clockwise to the horizontal direction as 0°, 60°, 120°, and 180°, respectively; (b) reproducing process of each category of units S_{0°, S_{60°, S_{120°, S_{180° in [N]th level from units in [$N-1$]th level; and (c) the number of segment in contact in each category of units. (n_f^c and n_s^c represent the numbers of flat and slant segments in contact, respectively.)

the load–displacement curves start from (0, 0) point. For the cases of $g > 0$, the curves show three stages: Stage I, $\delta < g$, the curve is with zero stiffness; Stage II, $2g < \delta < g$; and (3) Stage III, $\delta > 2\,g$. Fig. 6a also shows that when g increases, not only the contact of flat and slant segments is delayed, the slopes of the force displacement curves at stages II and III also decrease. To calculate the effective stiffness, the slope of force–displacement curve is converted to the slope of stress–strain curve by using initial area (w) and initial amplitude (L) of one Koch RVE (Fig. 4a). So that stiffness E_{II} and E_{III} of Stage II Stage III can be obtained, respectively.

To evaluate the effect of friction coefficient μ, the overall load–displacement curves for the cases of $N = 3$, $g = 0.1$ mm and $r_N = 0$ with different friction coefficient $\mu = 0$, 0.1, 0.2 and 0.3 are plotted in Fig. 6b. It can be seen that when μ increases, the slopes at Stage II are barely influenced, while the slopes at Stage III slightly increases. This confirms the fact that the contact between flat surfaces is independent of friction coefficient μ. However, the contact of slant surfaces (Stage III) depends on μ. When μ increases, contact force also increases.

The influences of N and gap g on the effective stiffness of the two contact stages are also studied via the analytical model. Fig. 7a shows that when $g = 0$, as N increases, theoretically, the effective slope of force–displacement always increases. In this case, there is only one recognizable stage for contact mechanism (which is a combination of Stages II and III together) because that both flat and slant segments are in contact from the very beginning.

However, in reality, g cannot be zero. Fig. 7b shows that for the cases of $\mu = 0.1$, $g = 0.1$ mm, and $r_N = 0.15a_N$ (*i.e.* c = 0.15), when $N < 5$, the initial slopes of F–δ curve increases with N; when N increases beyond 4, the slope starts decreasing and eventually becomes zero when N increases beyond 5. This is because that for non-zero g values, when N increases beyond a critical value, the contact area starts to decrease and eventually goes to zero due to loss of contact/interlocking, as illustrated in Fig. S2 of the supporting material S2. This effect is quantified by Eqs. S2.1–S2.4. For example, as shown in Fig. 7c, when g increases to 0.2 mm, according to the geometry and these equations, when N increase from 4 to 5, the contact area of the flat segments a_f decreases, as leads to the decrease of the slope of the load–displacement curve. Also, when N increase from 3 to 4 and beyond, the contact area of the slant segments a_s vanishes, therefore, from stage II to stage III, no change in slope is observed for the cases of $N = 4$ and beyond. It can be concluded that the gap g plays a significant role in determining the contact behavior of Koch fractal interlocking.

The theoretical prediction results indicate that the number of hierarchy N and the imperfection g are both very important for

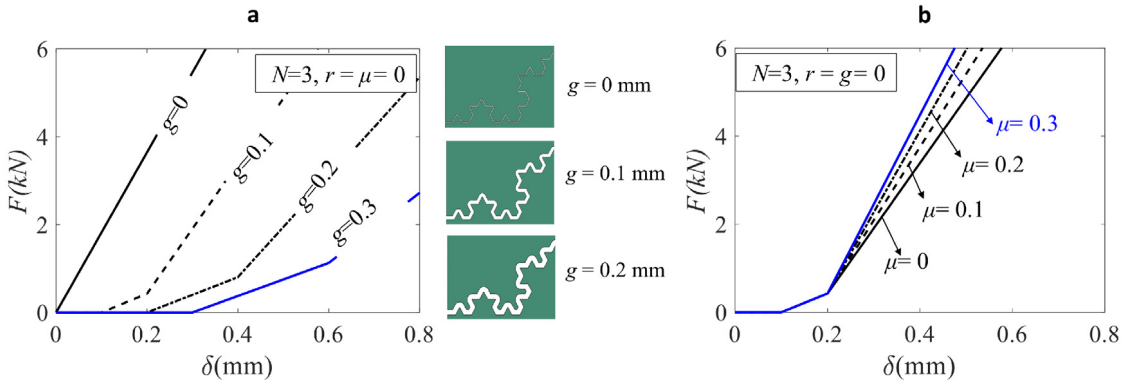

Fig. 6. Influence of (a) gap g and (b) friction coefficient μ on the mechanical response of Stages II and III for case $N = 3$ (the results shown are from the analytical model).

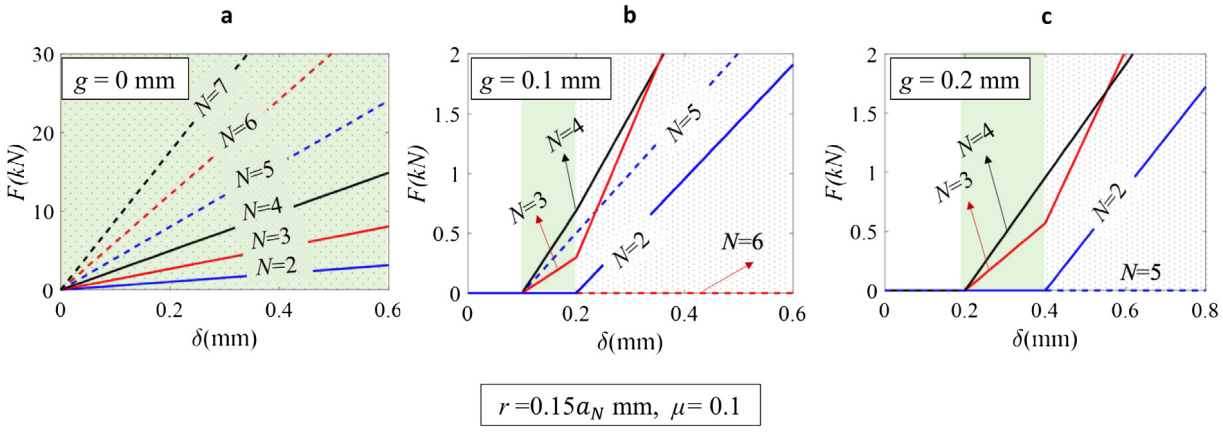

Fig. 7. Analytical prediction of the force displacement responses of Koch fractal interlocking with different orders of hierarchy N when (a) $g = 0$, (b) $g = 0.1$ mm (c) $g = 0.2$ mm. Each shaded area corresponds with one contact/interlocking stage.

the mechanical properties of the Koch fractal interlocking. Based on the theoretical model, the influences of N on the overall stiffness of E_{II} and E_{III} of the fractal interlocking at Stages II and III are plotted in Fig. 8a and c. To support the model prediction, FE results are also shown in Fig. 8a and c. It was found that E_{II} and E_{III} are functions of N, g, c and μ. The system of Eqs. (1)–(15) provides a scaling law to predict the influences of these parameters on E_{II} and E_{III}.

Fig. 8a shows that the influence of g on the non-dimensionalized effective stiffness of Stage II, $\frac{E_{II}}{E}$ for different N values, where E is the Young's modulus of the base material (VeroWhitePlus). The solid black curve indicates the stiffness of the perfect system of $g = 0$ and $r = 0$. It provides the upper limit of the effective stiffness for Koch contact for each N. For the perfect system, $E_{II} = E_{III}$, and they always increase with N. However, for any $g > 0$, and/or $c > 0$, there is a critical value of N_{cr} for each stage, when $N \geq N_{cr}$, the top and bottom piece will lose contact and have a zero stiffness. For example, for the cases shown in Fig. 8c, when $g = 0.1$ mm, $N_{cr} = 6$, and when $g = 0.2$ mm, $N_{cr} = 5$.

Fig. 8b shows an enlarged plot of Fig. 8a, when g changes from 0.01 to 0.1 mm. The figure shows that in this range, the stiffness changes more dramatically. It also shows that in Stage II, when g increases from 0.01 mm to 0.1 mm, N_{cr} decreases from 6 to 4. Also, in Stage II, the theoretical predictions of E_{II} are very consistent with FE results; while in Stage III, the FE results of E_{III} are lower than the theoretical prediction. This is due to the increasing in local deformation, such as the relative sliding between the slant surface and the bending of the small teeth in different hierarchies, which are not considered in the analytical model. Interestingly, when N increases from 3 to 4, the accuracy of analytical prediction increases. This is because that the local deformation for the case of $N = 4$ is smaller than that of $N = 3$, as was shown in Fig. 3c.

3. Conclusion and discussion

In summary, Koch fractal contact and interlocking were designed and fabricated via 3D printing. Through an integrated theoretical-numerical-experimental approach, we conclude that for Koch fractal interlocking, in order to reach optimal mechanical properties under desired design objectives, the geometric parameters N and gap g should be wisely and judiciously chosen. In general, for a perfect system, stiffness, strength and toughness increases when N increases. For a certain geometric imperfection, there is an optimal N for maximum overall stiffness.

Being consistent with the observation of fractal interlocks in nature, we demonstrated that in general the stiffness of the interlocking can be effectively increased via fractal design. In general, when the fractal complexity (it is specifically represented as number of hierarchy N in the present Koch fractal design) increases, the stiffness of the fractal interlocking will increase significantly [2]. This is mainly attributed to the increase in contact area when fractal complexity increases. However, the mechanical responses of fractal interlocks are also sensitive to imperfections, such as the gap between the interlocked pieces. When fractal complexity increases, the mechanical properties will become more and more sensitive to the imperfection and eventually, the negative influences from imperfection can even become dominant. Therefore, it is expected that considering the imperfection, there is an optimal level of fractal complexity to reach the maximum mechanical performance [54]. This is again in consistent with fractal interlocking in all different biological systems.

Due to the imperfection sensitivity of fractal design, the challenges of applying fractal design in engineering system are the

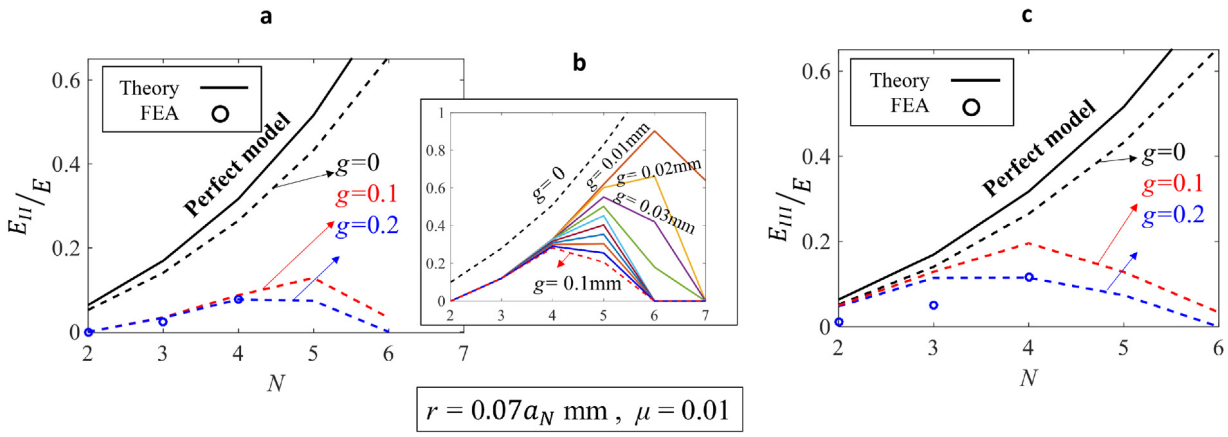

Fig. 8. (a) Influences of gap g on non-dimensionalized effective stiffness in Stage II; (b) enlarged plot of Figure (a) when g changes from 0.01 to 0.1 mm; and (c) the influences of gap g on non-dimensionalized effective stiffness in Stage III. (The solid black curves represent the ideal case of $g = 0$ and $r = 0$ which is the upper limit of effective stiffness for Koch contact for each N.)

complexity and accuracy in manufacturing. Additive manufacturing provides an opportunity to overcome these challenges and enable potential wide application of the concept of fractal design.

4. Methods

Experiments. All specimens were fabricated via a multi-material 3D printer (Objet Connex260). Two elastomers VeroWhitePlus (VW+, a hard acrylic plastic) and TangoBlackPlus (TB+, soft rubbery material) were used to fabricate the top/bottom pieces and interfacial layer (gap), respectively.

The dimensions of the specimens of Koch fractal interlocking are: the out of plane thickness is 4 mm, gap $g = 0.2$ mm, width of fractal zone $a_0 = 54$ mm, the tooth tip radius $r_N = 0.07a_N$ ($i.e.$ $c = 0.07$), the width of all specimens is $w = 75$ mm and total height of all specimen is $H = 210$ mm. Then the specimen was mounted on the Zwick material testing machine. Quasi-static load control experiments were performed with the uni-axial tensile loading rate of 0.024 mm/min.

Numerical simulations. All FE models were developed in ABAQUS /CAE V 6.13 (Simulia, USA) software. All FE simulations were performed in ABAQUS/Explicit. Both 2D and 3D FE models of the three specimens ($N = 2$, 3 and 4) were developed. For 2D models, quadrilateral plane stress elements (CPS4R) with reduced integration points were used. For 3D models, eight-node brick elements (C3D8R) with reduced integration point were used.

In all FE models, hard contact, with penalty algorithm was defined. Friction coefficient of $\mu = 0.01$ was used. The hard phase was modeled as elasto-perfectly plastic material with Young's modulus $E = 1700$ MPa, Poisson's ratio $\upsilon = 0.33$, yielding strength of $\sigma = 32$ MPa and density of $\rho = 1.1e^{-3}$ kg/mm^3. The adhesive layer is with the Young's modulus $E = 2$ MPa, Poisson's ratio $\upsilon = 0.4$, and ultimate strength $\sigma = 0.7$ MPa. These parameters were obtained from the mechanical experiment of the 3D printed material (details are provided in the Supporting information **S1**.). More information about the mechanical models and model parameters of the 3D printed materials can be found in [55–58].

Acknowledgments

This work was supported by National Science Foundation (NSF), USA under grant CMMI-1362893, US Air Force Office of Scientific Research (AFOSR), USA under grant FA9550-16-1-0011. The authors also acknowledge valuable comments from Professor James Barber at the University of Michigan, Ann Arbor.

Appendix A. Supplementary data

Supplementary material related to this article can be found online at https://doi.org/10.1016/j.eml.2018.09.003.

References

[1] U.G. Wegst, H. Bai, E. Saiz, A.P. Tomsia, R.O. Ritchie, Bioinspired structural materials, Nat. Mater. 14 (1) (2015) 23.
[2] Y. Li, C. Ortiz, M.C. Boyce, Bioinspired, mechanical, deterministic fractal model for hierarchical suture joints, Phys. Rev. E 85 (3) (2012) 031901.
[3] B.B. Mandelbrot, The fractal geometry of nature (Vol. 1), WH freeman, New York, 1982.
[4] F. Barthelat, Biomimetics for next generation materials, PPhil. Trans. R. Soc. A 365 (1861) (2007) 2907–2919.
[5] F. Barthelat, H. Tang, P.D. Zavattieri, C.M. Li, H.D. Espinosa, On the mechanics of mother-of-pearl: a key feature in the material hierarchical structure, J. Mech. Phys. Solids 55 (2) (2007) 306–337.
[6] F. Barthelat, Nacre from mollusk shells: a model for high-performance structural materials, Bioinspiration & Biomimetics 5 (3) (2010) 035001.
[7] W.B. Saunders, D.M. Work, S.V. Nikolaeva, Evolution of complexity in paleozoic ammonoid sutures, Science 286 (5440) (1999) 760–763.
[8] E.G. Allen, Understanding ammonoid sutures: new insight into the dynamic evolution of paleozoic suture morpholog, in: Cephalopods Present and Past: New Insights and Fresh Perspectives, Springer, Dordrecht, 2007, pp. 159–180.
[9] R.A. Hewitt, G.E. Westermann, Mechanical significance of ammonoid septa with complex sutures, Lethaia 30 (3) (1997) 205–212.
[10] J.S. Kwak, T.W. Kim, A review of adhesion and friction models for gecko feet, Int. J. Precis. Eng. Manuf. 11 (1) (2010) 171–186.
[11] T.M. Lutz, G.E. Boyajian, Fractal geometry of ammonoid sutures, Paleobiology 21 (3) (1995) 329–342.
[12] Y. Li, C. Ortiz, M.C. Boyce, A generalized mechanical model for suture interfaces of arbitrary geometry, J. Mech. Phys. Solids 61 (4) (2013) 1144–1167.
[13] P.Y. Chen, A.Y.M. Lin, Y.S. Lin, Y. Seki, A.G. Stokes, J. Peyras, J. McKittrick, Structure and mechanical properties of selected biological materials, J. Mech. Behav. Biomed. Mater. 1 (3) (2008) 208–226.
[14] T. Miura, C.A. Perlyn, M. Kinboshi, N. Ogihara, M. Kobayashi-Miura, G.M. Morriss-Kay, K. Shiota, Mechanism of skull suture maintenance and interdigitation, J. Anat. 215 (6) (2009) 642–655.
[15] J. Gibert, P. Palmqvist, Fractal analysis of the orce skull sutures, J. Human Evol. 28 (6) (1995) 561–575.
[16] M.M. Khoshhesab, Y. Li, The strength of dissimilar fractal joints, ASME/IMECE Proceeding. (2016) Paper number 66830.
[17] I.M. Rian, S. Asayama, Computational design of a nature-inspired architectural structure using the concepts of self-similar and random fractals, Autom. Constr. 66 (2016) 43–58.
[18] L. Wang, J. Lau, E.L. Thomas, M.C. Boyce, Co-continuous composite materials for stiffness, strength, and energy dissipation, Adv. Mater. 23 (13) (2011) 1524–1529.
[19] https://en.wikipedia.org/wiki/Fractal.
[20] D. Stoyan, H. Stoyan, Fractals, random shapes, and point fields: methods of geometrical statistics (Vol. 302), John Wiley & Sons Inc, 1994.
[21] Y. Li, C. Ortiz, M.C. Boyce, Stiffness and strength of suture joints in nature, Phys. Rev. E 84 (6) (2011) 062904.

[22] H.W. Chung, Y.H. Huang, Fractal analysis of nuclear medicine images for the diagnosis of pulmonary emphysema: interpretations, implications, and limitations, Am. J. Roentgenol. 174 (4) (2000) 1055–1059.
[23] B. Spehar, C.W. Clifford, B.R. Newell, R.P. Taylor, Universal aesthetic of fractals, Comput. Graphics 27 (5) (2003) 813–820.
[24] J.H. Brown, V.K. Gupta, B.L. Li, B.T. Milne, C. Restrepo, G.B. West, The fractal nature of nature: power laws, ecological complexity and biodiversity, Philos. Trans. R. Soc. B 357 (1421) (2002) 619–626.
[25] A. Jacquin, An introduction to fractals and their applications in electrical engineering, J. Franklin Inst. B 331 (6) (1994) 659–680.
[26] J.W. Baish, R.K. Jain, Fractals and cancer, Cancer Res. 60 (14) (2000) 3683–3688.
[27] M. Monsef Khoshhesab, Master thesis. Design, mechanical modeling and 3D printing of Koch fractal contact and interlocking, 2017.
[28] Y. Estrin, A.V. Dyskin, E. Pasternak, H.C. Khor, A.J. Kanel-Belov, Topological interlocking of protective tiles for the space shuttle, Philos. Mag. Lett. 83 (6) (2003) 351–355.
[29] K.L. Mittal, The role of the interface in adhesion phenomena, Polym. Eng. Sci. 17 (7) (1977) 467–473.
[30] R. Raj, M.F. Ashby, On grain boundary sliding and diffusional creep, Metall. Trans. 2 (4) (1971) 1113–1127.
[31] I.A. Malik, M. Mirkhalaf, F. Barthelat, Bio-inspired "jigsaw"-like interlocking sutures: Modeling, optimization, 3D printing and testing, J. Mech. Phys. Solids 102 (2017) 224–238.
[32] M.M. Khoshhesab, Y. Li, Mechanical modeling of fractal interlocking. ASME/IMECE Proceeding. Paper number 71845, 2017.
[33] L. Djumas, A. Molotnikov, G.P. Simon, Y. Estrin, Enhanced mechanical performance of bio-inspired hybrid structures utilising topological interlocking geometry, Sci. Rep. 6 (2016) 26706.
[34] M. Mirkhalaf, F. Barthelat, Design, 3D printing and testing of architectured materials with bistable interlocks, Extreme Mechanics Lett. 11 (2017) 1–7.
[35] P. Fratzl, O. Kolednik, F.D. Fischer, M.N. Dean, The mechanics of tessellations–bioinspired strategies for fracture resistance, Chem. Soc. Rev. 45 (2) (2016) 252–267.
[36] F. Barthelat, H. Tang, P.D. Zavattieri, C.M. Li, H.D. Espinosa, On the mechanics of mother-of-pearl: a key feature in the material hierarchical structure, J. Mech. Phys. Solids 55 (2) (2007) 306–337.
[37] Y. Zhang, H. Yao, C. Ortiz, J. Xu, M. Dao, Bio-inspired interfacial strengthening strategy through geometrically interlocking designs, J. Mech. Behav. Biomed. Mater. 15 (2012) 70–77.
[38] C. Gao, B.P. Hasseldine, L. Li, J.C. Weaver, Y. Li, Amplifying strength, toughness, and auxeticity via wavy sutural tessellation in plant seedcoats, Adv. Mater. (2018) 1800579.
[39] H. Tang, F. Barthelat, H.D. Espinosa, An elasto-viscoplastic interface model for investigating the constitutive behavior of nacre, J. Mech. Phys. Solids 55 (7) (2007) 1410–1438.
[40] S. Krauss, E. Monsonego-Ornan, E. Zelzer, P. Fratzl, R. Shahar, Mechanical function of a complex three-dimensional suture joining the bony elements in the shell of the red-eared slider turtle, Adv. Mater. 21 (4) (2009) 407–412.
[41] B.P. Hasseldine, C. Gao, J.M. Collins, H.D. Jung, T.S. Jang, J. Song, Y. Li, Mechanical response of common millet (panicum miliaceum) seeds under quasi-static compression: experiments and modeling, J. Mech. Behav. Biomed. Mater. 73 (2017) 102–113.
[42] S.W. Herring, Mechanical influences on suture development and patency, in: Craniofacial Sutures (Vol. 12, 41-56), Karger Publishers, 2008.
[43] C.R. Jaslow, A.A. Biewener, Strain patterns in the horncores, cranial bones and sutures of goats (Capra hircus) during impact loading, J. Zool. 235 (2) (1995) 193–210.
[44] A. Maloul, J. Fialkov, D. Wagner, C.M. Whyne, Characterization of craniofacial sutures using the finite element method, J. Biomech. 47 (1) (2014) 245–252.
[45] http://westerndiatoms.colorado.edus.
[46] L. Liu, Y. Li, Failure mechanism transition of 3D-printed biomimetic sutures, Eng. Fract. Mech. 199 (2018) 372–379.
[47] E. Lin, Y. Li, J.C. Weaver, C. Ortiz, M.C. Boyce, Tunability and enhancement of mechanical behavior with additively manufactured bio-inspired hierarchical suture interfaces, J. Mater. Res. 29 (17) (2014) 1867–1875.
[48] E. Lin, Y. Li, C. Ortiz, M.C. Boyce, 3D printed, bio-inspired prototypes and analytical models for structured suture interfaces with geometrically-tuned deformation and failure behavior, J. Mech. Phys. Solids 73 (2014) 166–182.
[49] E.E.S. Lin, Bio-inspired design of geometrically-structured suture interfaces and composites, (Doctoral dissertation), Massachusetts Institute of Technology, 2015.
[50] F. Barthelat, Z. Yin, M.J. Buehler, Structure and mechanics of interfaces in biological materials, Nat. Rev. Mater. 1 (4) (2016) 16007.
[51] L. Liu, Y. Jiang, M. Boyce, C. Ortiz, J. Baur, J. Song, Y. Li, The effects of morphological irregularity on the mechanical behavior of interdigitated biological sutures under tension, J. Biomech. 58 (2017) 71–78.
[52] P.J. Ryan, Euclidean and Non-Euclidean Geometry: An Analytic Approach, Cambridge university press, 1986.
[53] Paul S. Addison, Fractals and Chaos: An Illustrated Course. Institute of Physics. ISBN 0-7503-0400-6, 1997.
[54] R.H. Dauskardt, F. Haubensak, R.O. Ritchie, On the interpretation of the fractal character of fracture surfaces, Acta Metall. Mater. 38 (2) (1990) 143–159.
[55] Y. Jiang, Y. Li, 3D Printed Auxetic mechanical metamaterial with chiral cells and re-entrant cores, Sci. Rep. 8 (1) (2018) 2397.
[56] Y. Jiang, Y. Li, Novel 3D-printed hybrid auxetic mechanical metamaterial with chirality-induced sequential cell opening mechanisms, Adv. Energy Mater. 20 (2) (2018) 1700744.
[57] Y. Jiang, Y. Li, 3D printed chiral cellular solids with amplified auxetic effects due to elevated internal rotation, Adv. Energy Mater. 19 (2) (2017) 1600609.
[58] L. Liu, Y. Li, Predicting the mixed-mode I/II spatial damage propagation along 3D-printed soft interfacial layer via a hyperelastic softening model, J. Mech. Phys. Solids 116 (2018) 17–32.